Check for updates

Recovering carbon losses in CO_2 electrolysis using a solid electrolyte reactor

Jung Yoon 'Timothy' Kim [1,5], Peng Zhu [1,5], Feng-Yang Chen [1], Zhen-Yu Wu [1], David A. Cullen [2] and Haotian Wang [1,3,4] ✉
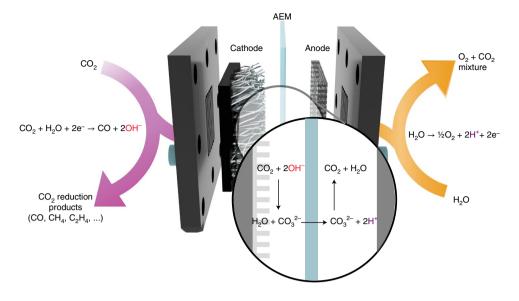
The practical implementation of electrochemical CO_2 reduction technology is greatly challenged by notable CO_2 crossover to the anode side, where the crossed-over CO_2 is mixed with O_2, via interfacial carbonate formation in traditional CO_2 electrolysers. Here we report a porous solid electrolyte reactor strategy to efficiently recover these carbon losses. By creating a permeable and ion-conducting sulfonated polymer electrolyte between cathode and anode as a buffer layer, the crossover carbonate can combine with protons generated from the anode to re-form CO_2 gas for reuse without mixing with anodic O_2. Using a silver nanowire catalyst for CO_2 reduction to CO, we demonstrated up to 90% recovery of the crossover CO_2 in an ultrahigh gas purity form (>99%), while delivering over 90% CO Faradaic efficiency under a 200 mA cm^{-2} current. A high continuous CO_2 conversion efficiency of over 90% was achieved by recycling the recovered CO_2 to the CO_2 input stream.

As the facilitation and distribution of renewable electricity become the viable alternative to fossil fuels, electrochemically converting carbon dioxide back into basic chemical feedstocks has been perceived by numerous researchers as a promising method for storing and using this renewable electricity while mitigating climate change[1–4]. Tremendous efforts and noticeable advancements were made in the CO_2 reduction reaction (CO_2RR) in the past few decades targeting high efficiency and selectivity towards desired products[5–8]. Among these efforts, catalytic materials design and reactor engineering have been the two main ones in the field[9–11]. While a wide range of catalysts have been developed to improve intrinsic CO_2RR selectivity and activity towards C_1 (CO, formate, methanol, methane)[12–18], C_2 (ethylene, ethanol, acetate)[19–21] and even C_3 (n-propanol) products[22,23], the developments in CO_2 electrolysers, especially the use of gas diffusion layer (GDL) electrodes in flow cell and membrane electrode assembly (MEA) cell reactors, play a central role in pushing the catalytic performance towards industrially relevant metrics[24–27]. Using CO_2 reduction to CO in a MEA cell as a representative example, the current density and CO selectivity can now reach a few hundreds of mA cm^{-2} and over 90% Faradaic efficiency (FE) on several selective catalysts (such as Ag nanoparticles (NPs)[28], transition metal single atom catalysts (SACs)[12,29,30] and so on), setting up a solid foundation for possible industrialization in the future.

As promising as these advances in CO_2RR performance are, there is, however, a fundamental but often overlooked challenge that could dramatically limit the commercialization potential of CO_2RR technology: the subtantial carbon loss due to carbonate crossover (Fig. 1). During CO_2RR electrolysis, especially under large current densities, large numbers of hydroxide ions (OH$^-$) are generated at the cathode–electrolyte interface, which react rapidly with the CO_2 stream to form carbonate or bicarbonate ions[25,31–42]. These carbonate ions, driven by the electrical field, then migrate across the cathode–anode interface (either aqueous solutions or anion exchange membranes) towards the anode side of the reactor, and are recombined with the locally generated protons (H$^+$) from the oxygen evolution reaction (OER) to form CO_2 gas again (Fig. 1). Unfortunately, these crossover CO_2 gas molecules cannot be directly reused for CO_2RR as they are in a mixture with the anode O_2, resulting in a notable carbon loss that dampens the overall energy efficiency of CO_2RR technology[25,32–41]. The carbon loss problem is even more severe when strong alkaline solutions are used due to the continuous chemical reaction between the CO_2 stream and electrolyte[31,32,34,36,39,40].

Researchers started to realize and point out this CO_2 crossover challenge in CO_2RR technology in recent studies[32–34,36,39,40,42–44]. However, only a few known studies were able to propose industrially and economically viable solutions to address this carbonate crossover issue. Using a strong acid electrolyte, a proton exchange membrane MEA (PEM, such as Nafion) or a bipolar membrane MEA (cation exchange side facing the CO_2RR cathode) could prevent the CO_2 crossover, but their applications are limited by low CO_2RR selectivity due to strong competition from the hydrogen evolution reaction (HER) or low operation stability, if without specific interfacial engineering[11,43,44]. One representative example of this interfacial engineering was recently demonstrated by Sargent's group where the concentrated potassium ions at the catalyst–PEM interface can largely improve CO_2RR performance in PEM and mitigate the CO_2 crossover[43]. Here we demonstrate a high-efficiency recovery of the crossover CO_2 during CO_2RR electrolysis using a porous solid electrolyte (PSE) reactor design. By introducing a sulfonated polymer electrolyte buffer layer between cathode and anode, crossover CO_3^{2-} could combine with protons (from anode OER) to form CO_2 gas again, which can be easily recaptured by continuously flushing the PSE layer with deionized (DI) water. Using Ag nanowire (NW) catalyst as a model study, we consistently recovered over 90% of the crossover CO_2 gas in an ultrahigh purity form (over 99% gas purity), while maintaining a decent CO_2RR catalytic performance of over 90% CO selectivity and high current density of 200 mA cm^{-2}. We also demonstrated that this PSE reactor design for crossover CO_2 recovery can be successfully extended to different CO_2RR catalysts and products. Furthermore, we were able to recycle this recovered CO_2 back to the input stream to obtain

[1]Department of Chemical and Biomolecular Engineering, Rice University, Houston, TX, USA. [2]Center for Nanophase Materials Science, Oak Ridge National Laboratory, Oak Ridge, TN, USA. [3]Department of Materials Science and NanoEngineering, Rice University, Houston, TX, USA. [4]Department of Chemistry, Rice University, Houston, TX, USA. [5]These authors contributed equally: Jung Yoon 'Timothy' Kim, Peng Zhu. ✉e-mail: htwang@rice.edu

Fig. 1 | Schematic of CO₂ crossover phenomenon in anionic MEA cells. Schematic of CO_2RR MEA setup, showing how CO_2 from the cathode crosses past the anion exchange membrane into the anode via its reaction with hydroxide ions (in red) and protons (in purple).

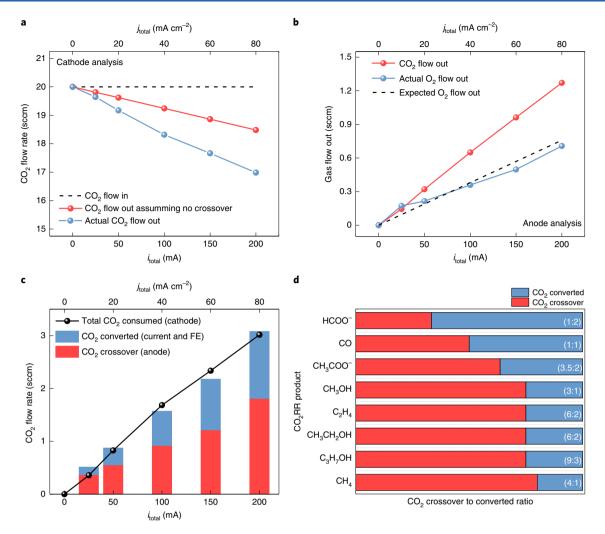a high continuous CO_2 conversion efficiency of over 90% under 100 mA cm⁻² current density.

Results

CO₂ crossover in traditional CO₂RR electrolysers. Since the CO_2 crossover rates are typically at the same orders of magnitude with CO_2 reduction rates, which are usually much lower (under small currents) than the CO_2 stream flow rates used in CO_2RR experiments, this CO_2 crossover phenomenon would not introduce much error during the quantification of gas product FEs, and thus has often escaped researchers' notice. To validate and also systematically quantify the CO_2 crossover problem, here we used a commercial Ag NW catalyst in a standard anion MEA cell for 2e⁻ CO_2 reduction to CO (Fig. 2 and Methods). Ag NW was selected for its commercial availability, good selectivity and stability towards CO_2 electroreduction to CO. Other Ag-based catalysts such as Ag NPs showed similar catalytic performances to Ag NWs for both MEA and PSE reactors (Supplementary Fig. 1), suggesting that our choice of this NW catalyst did not have specific motives besides the NW's availability in our laboratory. The electrode geometric surface area we used is 2.5 cm² and the CO_2 upstream (input) flow rate was set at 20 standard cubic centimetres per minute (sccm) by a mass flow controller (MFC) across this work unless specifically noted. The current–voltage (*IV*) curves of the MEA cell and gas product FEs are included in Supplementary Fig. 2, with CO as the dominant product[45–47]. The crossover CO_2 can be either directly measured by analysing the gas output flow on the anode side (O_2 + CO_2), or indirectly measured by analysing the CO_2 output rate and conversion rate (crossover = input − output − conversion). The corresponding experimental setups for gas analysis will be discussed in detail in Fig. 3b, Methods and Supplementary Fig. 3. First, the cathode-side CO_2 downstream gas analysis (Fig. 2a) shows that the actual CO_2 consumption rate (20 sccm minus downstream flow rate) well exceeds the CO_2-to-CO conversion rate (calculated on the basis of CO partial current, Methods). In fact, the results showed that approximately the same amount of CO_2 was lost compared to the amount of CO_2 that gets reduced to form CO products under a wide range of cell currents, suggesting a substantial carbon loss issue with a low CO_2 use efficiency of roughly 50%. On the anode side, besides the expected O_2 gas produced from OER, there is a large amount of CO_2 flow detected (Fig. 2b). The natural diffusion of CO_2 gas

across the anion exchange membrane (AEM) can be ruled out since we did not observe any CO_2 gas flow on the anode side when no currents were applied on the cell. It is encouraging to find out that the CO_2 flow rate measured from the anode side, added together with the CO_2-to-CO conversion rate, matches well with the total CO_2 consumption rate measured from the cathode side (Fig. 2c). The agreement between these three independent measurements suggests a high accuracy of our experimental design in carbon balance analysis. With this, we have concluded that a large portion of CO_2 gas used in this system is crossed over to the other side and is mixed with oxygen gas, resulting in notable energy loss and cost increase in CO_2RR process. By taking a closer look at the CO_2 crossover rate (especially under larger currents where measurements are more accurate), we noticed that it is similar to the CO generation rate and is approximately double the O_2 generation rate. This correlation strongly indicates that the CO_2 crossover is mainly through the carbonate ions (CO_3^{2-}) instead of bicarbonate (Fig. 1)[25,32–34,36]: for every two electrons transferred in CO_2RR, there will be two OH⁻ groups generated to form one carbonate group (except for anionic products such as formate or acetate). The result agrees well with thermodynamics equilibria that show the hydroxide and CO_2 interaction at the catalyst–AEM interface mostly results in carbonate instead of bicarbonate ions due to strong alkaline local pH during CO_2RR electrolysis at the cathode[25,34,36]. On the basis of this principle, the CO_2 crossover problem is exacerbated when higher-value products are targeted (Fig. 2d and Table 1). For example, for every two CO_2 molecules converted to a C_2 product of ethylene, there will be six CO_2 molecules crossing over to the anode side (crossover to conversion ratio of 3 to 1), which lowers the CO_2 use efficiency to only 25%. Even worse, this 25% efficiency is only a theoretical upper limit when the C_2H_4 FE is 100%. The competitive HER and other side products will further increase the CO_2 crossover rate and bring down the CO_2 use efficiency in CO_2RR electrolysis.

PSE reactor system design for crossover CO₂ recovery. As it is extremely difficult to prevent the formation and crossover of carbonate ions at the catalyst–AEM interface, the strategy we propose is to create a buffer layer between cathode and anode that could neutralize formed carbonate ions to regenerate CO_2 gas before they reach the anode side. There are a few prerequisites of this buffer layer to serve the CO_2 recovery purpose. First, it must have high ionic conductivity
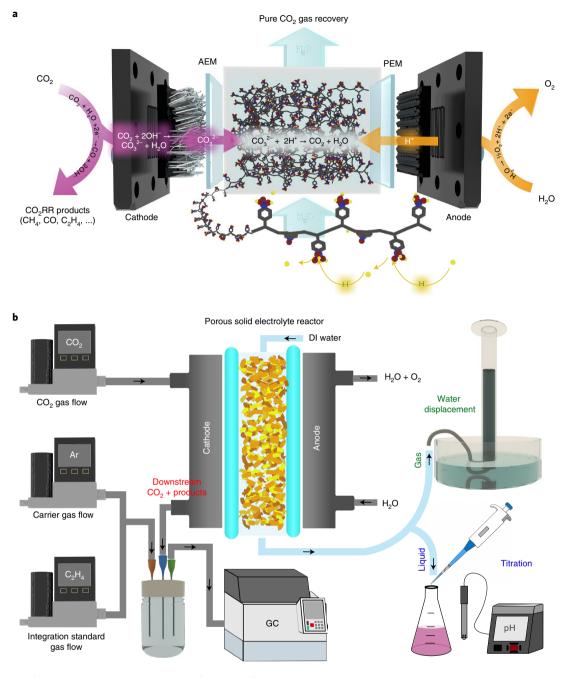
Fig. 2 | Substantial carbon loss in traditional CO_2 MEA electrolysers. a, CO_2 flow analysis of the cathode side in which actual CO_2 flow out (blue) is much less than CO_2 flow, which considers only CO_2RR consumption (red). **b**, Total gas flow analysis of the anode side in which electrochemically calculated O_2 flow (dashed line) and measured O_2 flow out (blue) are far exceeded by the crossover CO_2 gas flow (red). **c**, CO_2 flow analysis that shows the crossover CO_2 (from anode gas analysis) and the CO_2 converted (from partial current of CO_2), which adds up to match the total CO_2 flow change well (the difference between the CO_2 inlet and the downstream CO_2) on the cathode side. **d**, Ratio of crossover CO_2 to converted CO_2 for different CO_2RR products. This ratio is calculated with the assumption of 100% FE towards the specific target product.

that can ensure a small ohmic drop between cathode and anode for high energy efficiencies. Second, its pH should be at around neutral range (such as CO_2 saturated water with pH 5), as high alkaline pH greatly increases the CO_2 crossover rate due to carbonate formation, and low acidic pH could damage the AEM and lower the CO_2RR catalytic performances. Third, it must not be continuously consumed by reacting with crossover CO_2, which makes the system unsustainable. At first glance, a specific liquid electrolyte such as $NaHCO_3$ or $KHCO_3$ solution seems to be able to serve the purpose. However, as the solubility of these bicarbonate salts is typically within a few moles per litre, and ion conduction is mainly conveyed by Na^+ or K^+ ions that are far slower compared to protons[48], their ion conductivity is dramatically limited. The liquid electrolyte is also mixed with the CO_2RR liquid products such as formic acid or ethanol during the operation, which adds another separation step to obtain high purity liquid products. More importantly, concentrated liquid electrolyte is known to negatively affect the stability of CO_2RR due to the salt precipitation on the cathode electrode that blocks CO_2 diffusions[49,50].

Our design of a PSE layer as the buffer layer could satisfy the above-mentioned requirements and avoid the challenges that liquid electrolytes are faced with. As shown in Fig. 3a, the solid electrolyte

layer contains dense but permeable ion-conducting polymers functionalized with sulfonate groups, which guarantees efficient proton conductions (like a Nafion membrane does) between cathode and anode with a voltage comparable to that of an MEA device (cell assembly in the Methods and Supplementary Fig. 4)[51–55]. Taking notice of the aforementioned carbonate crossover phenomenon in MEA, we proposed that a similar process would be taking place at the cathode in our solid electrolyte reactor design. We speculated that the solid electrolyte device's cathode-side CO_2RR will result in the formation of hydroxide ions, which will then react with free CO_2 gas to form carbonate ions. These carbonate ions would be driven by the electrical field to migrate across the AEM into the solid electrolyte layer, where they are recombined with protons generated from the anodic OER to compensate for the charge. Therefore, our solid electrolyte buffer layer serves as a recombination site for carbonate and protons, while not sacrificing CO_2RR performances as demonstrated in our previous solid electrolyte reactor systems[51–55]. The protonation of carbonate results in the formation of dissolved CO_2 and CO_2 gas, which are now completely separated from the anode O_2 stream. By recycling a DI water stream (saturated by CO_2) through this PSE layer to push out regenerated CO_2 gas, we can

Fig. 3 | PSE reactor design for crossover CO₂ recovery and its gas analysis system. a, Schematic of CO₂RR in the PSE reactor and recovery process of crossover CO_3^{2-} ion by recombination with protons in the PSE buffer layer. The protons generated from the anode side move across the PEM then hop across the solid electrolyte efficiently via sulfonate functional groups as shown with the yellow arrows. **b**, Schematic of CO₂ recovery measurement during CO₂RR process in the PSE reactor. One independent GC measurement is conducted on the cathode-side downstream gas flow and two independent measurements, titration and water displacement, are conducted on the middle-layer downstream flow.

realize a continuous recovery of ultrahigh purity CO_2 gas that can be readily reused in CO_2RR.

To validate this idea and to evaluate the CO_2 recovery capability of our PSE reactor, an accurate measurement of CO_2 crossover rate and CO_2 recovery rate is of central importance. First, on the cathode side, the input 20 sccm CO_2 stream will be split into three components: converted CO_2 (to CO), crossover CO_2 (to solid electrolyte layer) and remaining downstream CO_2. To obtain the CO_2 crossover rates under different cell operation conditions, we will then need to measure the CO_2 conversion rates and downstream CO_2 flow rates. While the CO_2 conversion rates can be easily

calculated on the basis of the CO/H_2 quantification using gas chromatography (GC) and the cell current (Methods), the measurement of downstream CO_2 flow rates is challenging due to the small flow rate changes compared to its baseline, especially under low cell currents. One straightforward method is to directly connect the downstream to another MFC and translate its flow rate readings back to CO_2 flow rate by considering the generated CO and H_2 gas components, but when the measurement was compared with the titrated CO_2 quantity, we saw it deviated from its set point (Supplementary Fig. 5). Here we developed a more sophisticated and reliable gas analysis system, an internal gas standard strategy, for downstream CO_2

Table 1 | CO$_2$ reduction half-cell reactions and their corresponding CO$_2$ maximal use efficiency assuming 100% product selectivity

Electrochemical CO$_2$RR reactions	Maximal CO$_2$ use efficiency
$2H_2O(l) + 2e^- \rightarrow H_2(g) + 2OH^-$	N/A
$CO_2(g) + H_2O(l) + 2e^- \rightarrow HCOO^-(aq) + OH^-$	67%
$CO_2(g) + H_2O(l) + 2e^- \rightarrow CO(g) + 2OH^-$	50%
$2CO_2(g) + 5H_2O(l) + 7e^- \rightarrow CH_3COO^-(aq) + 7OH^-$	36%
$CO_2(g) + 5H_2O(l) + 6e^- \rightarrow CH_3OH(l) + 6OH^-$	25%
$2CO_2(g) + 8H_2O(l) + 12e^- \rightarrow C_2H_4(g) + 12OH^-$	25%
$2CO_2(g) + 9H_2O(l) + 12e^- \rightarrow CH_3CH_2OH(l) + 12OH^-$	25%
$CO_2(g) + 6H_2O(l) + 8e^- \rightarrow CH_4(g) + 8OH^-$	20%

flow rate measurements as shown in Fig. 3b. Before cathode-side downstream gas flow is fed into the GC, it is mixed with 200 sccm of Ar as a carrier gas and 5 sccm of the internal integration standard gas. Ethylene (C$_2$H$_4$) is mostly used as the internal integration standard gas, while methane (CH$_4$) is used for the systems where CO$_2$RR products includes C$_2$H$_4$ such as the Cu catalyst (no CH$_4$ is produced in our case). The ratio between CO$_2$ GC peak area to internal standard GC peak area was precalibrated for accurate measurements of the downstream CO$_2$ flow rate independent of complicated gas components in it (Methods and Supplementary Fig. 6).

Second, the crossover CO$_2$ gas will be dissolved in DI water before it emits as gas bubbles when water starts to get saturated. To most accurately measure the CO$_2$ crossover rate into the solid electrolyte layer, we chose to measure dissolved CO$_2$ and CO$_2$ gas bubbles in the DI water flow stream separately using titration and water displacement method, respectively (Fig. 3b and Methods). Please note here that the CO$_2$ dissolution in DI water stream will be avoided in practical operations when we continuously circulate the saturated DI water in our PSE layer, therefore all crossover CO$_2$ can be collected in its gas phase (demonstrated in our following long-term stability test). A titration method was used to accurately detect the amount of dissolved crossover CO$_2$ of all forms (carbonic acid, carbonate, bicarbonate and dissolved CO$_2$ equilibriums) within the DI water flow through the middle layer (Methods and Supplementary Figs. 7 and 8)[56]. Excessive crossover CO$_2$ was pushed out in its gas phase when the DI water stream got saturated, especially under large operation currents, and its volumetric flow rate was reliably measured using a water displacement method optimized for CO$_2$ gas (Methods and Supplementary Fig. 9)[57].

Characterizations of crossover CO$_2$ recovery. We used the same Ag NW CO$_2$-to-CO catalyst as in our MEA test on the cathode of our PSE reactor as a model case study of CO$_2$ recovery (Fig. 4a). An IrO$_2$ anode electrode was used on the other side to oxidize water to O$_2$ and to continuously supply protons to the solid electrolyte layer across the PEM (Methods). As shown from the scanning electron microscopy (SEM) and the high-resolution transmission electron microscopy (HRTEM) images in Fig. 4a and Supplementary Fig. 10, the Ag NWs present a uniform diameter of roughly 70 nm. The lattice spacing and the structure in the HRTEM shows that the surface of the Ag NW is mainly covered by a (111) facet, which was identified as the active surface for CO$_2$RR to CO in previous studies[46]. The *IV* curve of the solid electrolyte reactor, with an extra middle layer introduced, presents a similar CO$_2$RR activity compared to the MEA device (Fig. 4b and Supplementary Fig. 2). The CO$_2$RR selectivity of the solid electrolyte reactor was also comparable if not better than the MEA, with CO FE of roughly 90% under high currents

of up to 500 mA or 200 mA cm^{-2} (Fig. 4c and Supplementary Fig. 2). No other CO$_2$RR products were observed. Figure 4d presents the capability of our solid electrolyte reactor design to recover crossover CO$_2$ in the middle chamber during the CO$_2$RR to CO electrolysis. The theoretical guideline was calculated on the basis of the assumption that every two electrons transferred on the cathode will result in the generation of two OH$^-$ and thus absorb one CO$_2$ molecule to form one crossover CO$_3^{2-}$, therefore it is only related to the operation current and is independent of CO$_2$RR or HER FEs except for the generation of formate or acetate as crossover anions (Table 1). It is encouraging to observe that the CO$_2$ crossover rates we measured on the cathode side, which equal the total CO$_2$ consumption rate (input–output) minus the CO$_2$ conversion rate (to CO in this case), are very close to the theoretical ones under a wide range of cell operation currents, suggesting a high accuracy of our gas analysis system specifically designed for this carbon balance study. Although the discrepancies are small between these two values, it is also interesting to find out that our measured CO$_2$ crossover rates are always slightly higher than the theoretical guideline. This is possibly due to the potential gas leakage in our cell assembly or tube connections, which results in an underestimated downstream CO$_2$ flow rate and thus an overestimated CO$_2$ crossover rate.

The CO$_2$ recovery rate measured in the middle solid electrolyte layer, which consists of both dissolved CO$_2$ and gas-phase CO$_2$, continuously increased with the cell current (Fig. 4d). Under small operation currents, we observed that the dissolved CO$_2$ measured by titration was higher than the CO$_2$ bubble collection as the DI water stream was not yet saturated. Under higher cell currents, while we observed continuous increase in collected CO$_2$ bubbles, the rate of dissolved CO$_2$ reached a plateau of roughly 1 sccm (Supplementary Fig. 8). Considering our DI water flow rate was fixed at 1.1 ml min^{-1} through the solid electrolyte layer, this plateau suggested a CO$_2$-saturated DI water stream at roughly 0.91 ml$_{CO_2}$/ml$_{H_2O}$ under our operation conditions, which agrees very well with theoretical CO$_2$ solubility in water[56,58]. We want to emphasize here again that all the crossover CO$_2$ can be recovered in gas phase only in practical operations once we continue to recycle the saturated DI water stream (demonstrated below). The cell continuously recovered the total CO$_2$, both dissolved and gas bubbles, of up to 90% of the cathode-side measured crossover CO$_2$ quantity or roughly 100% of the theoretically calculated crossover CO$_2$ quantity across a wide range of operation currents (Fig. 4e). This small discrepancy in CO$_2$ recovery efficiencies can also be well explained by the above-discussed hypothesis that our measured CO$_2$ crossover rates could be slightly overestimated. The gas purity of our recovered CO$_2$ stream was above 99% as confirmed by GC measurements (Fig. 4f, Supplementary Fig. 11 and Methods), with only trace amounts of impurities including H$_2$ and O$_2$ that may come from electrolysis or air leakage.

A detailed comparison of the *IV* curves between our solid electrolyte reactor and the MEA cell, with most of the electrolyser components kept the same (Methods), is shown in Supplementary Figs. 12 and 13. The introduction of the extra solid electrolyte layer showed an impedance increase (roughly 1 Ω) compared to the MEA reactor, resulting in an additional 0.3 to 0.4 V cell voltage under the current density of 100 mA cm^{-2}. However, this voltage penalty can be reduced to only 0.15 V by thinning the solid electrolyte layer from 2.5 to 1.5 mm, which resulted in smaller resistance-caused voltage drops (also known as iR drops; Supplementary Fig. 13), suggesting that the cell voltage could be further improved when the thickness of the solid electrolyte layer is further reduced. Our technoeconomic analysis suggests that the energy penalty we paid in adding an extra layer of solid electrolyte to MEA for CO$_2$ recovery during the Ag NW CO$_2$RR is smaller than the energy consumptions needed to have a downstream CO$_2$/O$_2$ gas separation in the case of MEA operation of the Ag NW CO$_2$RR (Supplementary Note 1). Furthermore, the comparison seen in Supplementary Figs. 12

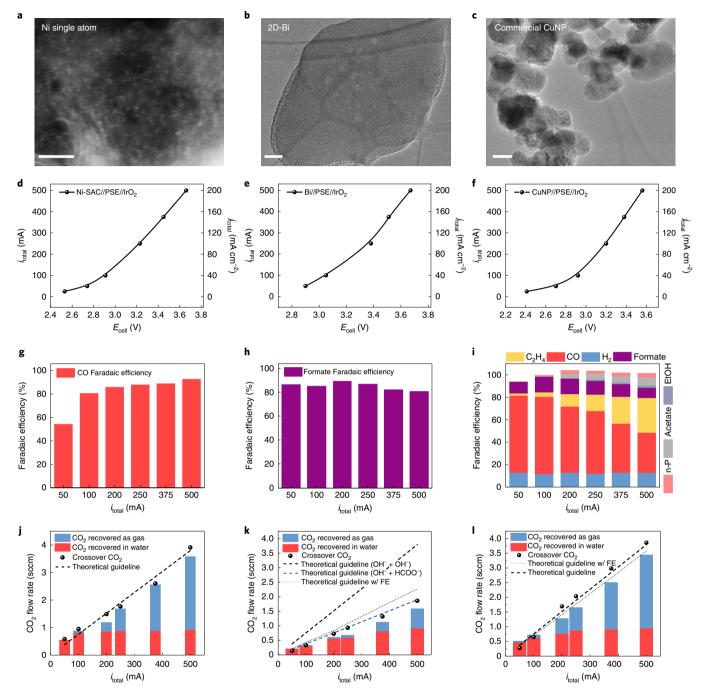**Fig. 4 | Crossover CO₂ recovery characterization in an Ag NW solid electrolyte reactor. a**, SEM (left) and HRTEM (right) image of Ag NW. Lattice spacing of 0.242 nm and the lattice structure shows that the (111) facet is the most prominent lattice on the surface of the NWs. **b**, The *IV* curve of CO₂RR on Ag NW catalyst in our solid electrolyte reactor. **c**, CO FE of Ag NW under different operation currents in our solid electrolyte reactor. **d**, The CO_2 recovery performance of solid electrolyte reactor using Ag NW. Gas recovery, dissolved liquid, crossover CO_2 and theoretical values were measured/calculated by water displacement, titration, GC measurement and applied current, respectively. **e**, Proportion of CO_2 recovered in the middle layer compared to the GC measured crossover CO_2 or the theoretically calculated crossover CO_2. **f**, Thermal conductivity detector response from the GC showing H_2 peak (roughly 0.52 min), O_2 peak (roughly 0.6 min) and CO_2 peak (roughly 2.3 min) with CO_2 corresponding purity of recovered gas for a range of currents. Scale bars in **a**, 500 nm (left) and 1 nm (right).
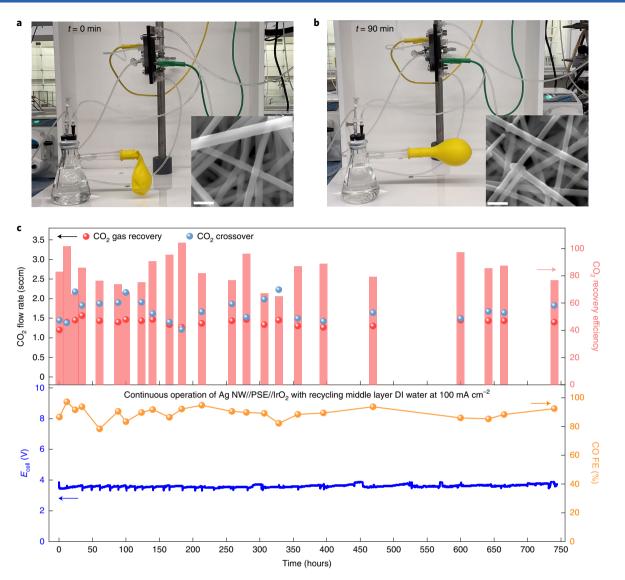
and 13 shows that the MEA device needs to operate with a liquid electrolyte, whereas the PSE device can be operated entirely with water. The ultrahigh purity of recovered CO_2 stream, high recovery efficiencies and similar CO_2RR selectivity compared to MEA suggest the great potential of our PSE reactor design in addressing the carbon loss challenge in practical CO_2 electrolysis.

Fig. 5 | The wide applicability of crossover CO_2 recovery using PSE reactor. CO_2RR and CO_2 recovery performance of Ni-SAC, 2D-Bi and CuNP: three different catalysts with unique CO_2RR selectivity. **a–c**, TEM of Ni-SAC (**a**), 2D-Bi (**b**) and CuNPs (**c**). **d–f**, Currents and current densities versus cell voltage (*IV* curves) of our PSE reactor with Ni-SAC (**d**), 2D-Bi (**e**) and CuNPs (**f**). **g–i**, CO FE, formate FE and seven different CO_2RR products FE during electrochemical testing in a solid electrolyte reactor with Ni-SAC (**g**), 2D-Bi (**h**) and CuNPs (**i**), respectively. **j–l**, CO_2 recovery performance for PSE reactor with Ni-SAC (**j**), 2D-Bi (**k**) and CuNPs (**l**). In 2D-Bi recovery performance, the topmost theoretical guideline ($OH^- + OH^-$) represents the same guideline shown for other CO catalysts, while the blue dashed theoretical guideline ($OH^- + HCOO^-$) demonstrates the crossover expectation (assuming 100% formate FE) when one formate ion replaces one hydroxide ion formed at the interface. The dotted theoretical guideline represents the crossover value when considering the actual formate FE. Likewise, the dotted theoretical line in CuNP considers the formation and crossover of formate and acetate as anionic products. Scale bars in **a**, 2 nm; **b**, 100 nm and **c**, 50 nm.

CO_2 gas recovery for different catalysts and CO_2RR products.

To demonstrate its general applicability, we further evaluated the CO_2 recovery performances of our PSE design with different CO_2RR catalysts and products. First, to investigate the possibility of using different CO_2 to CO catalysts for the same recovery design, a

Ni-SAC was used as it has been demonstrated to have high selectivity for CO in our and others' previous studies[59–63]. The TEM and SEM characterizations in Fig. 5a and Supplementary Fig. 14 confirmed the well-dispersed Ni single atoms in a carbon matrix. The CO_2RR-to-CO performance of Ni-SACs demonstrated previously
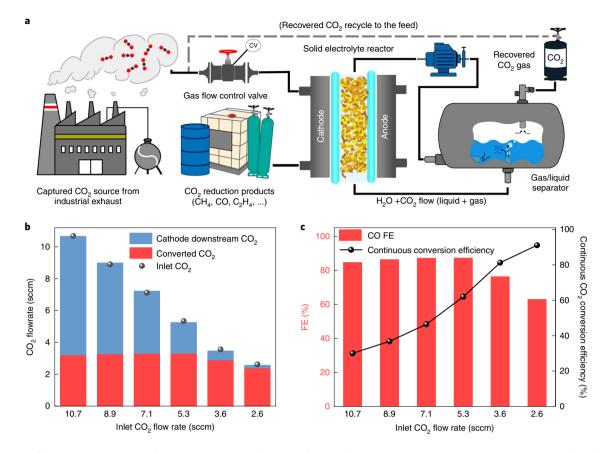
Fig. 6 | DI water recycling and stability test for continuous CO$_2$ gas recovery. a, Image of our solid electrolyte reactor system for CO$_2$ gas recovery and the SEM image of the Ag NW catalyst (inset) before cell operation. **b**, After 90 min of cell operation at 250 mA (100 mA cm^{-2}), a 100-ml balloon was filled up by recovered CO$_2$. The As NW catalyst did not show any structure change after catalysis. **c**, CO$_2$ recovery stability test under 250 mA or 100 mA cm^{-2} for 750 h. The cell voltage (blue) was stable throughout the test. Also, the CO FE percentage (orange) shows the device's ability to maintain high CO FE for long-term operation. CO$_2$ crossover rate measured with GC (red data points) and CO$_2$ recovery rate measured with the water displacement method (blue data points) showed no decay, with an average of 80–90% recovery (magenta) of the crossover CO$_2$ during 750 h of operation of our solid electrolyte reactor. Scale bars in **a** and **b**, 200 nm.

in a traditional electrolyser was successfully translated in our solid electrolyte reactor, which delivered industrially relevant currents (up to 500 mA or 200 mA cm^{-2}) while maintaining over 90% CO FE (Fig. 5d,g). Similar CO$_2$ crossover and recovery rates were observed as shown in Fig. 5j compared to the case of Ag NW, confirming that the carbon loss and recovery mechanisms were not related to the type of catalyst we used in the case of CO generation.

The CO$_2$ crossover rates could be dramatically different in the case of producing anionic CO$_2$RR products such as formate, since fewer OH$^-$ groups are generated (Fig. 2d and Table 1). To validate this hypothesis and to test the CO$_2$ recovery capability under this scenario, we changed the cathode catalyst to a two-dimensional Bi (2D-Bi) nanosheet catalyst (Fig. 5b and Supplementary Fig. 15), which has been demonstrated in our previous study to be highly selective for formic acid[53,64]. As expected, 2D-Bi showed high activity and selectivity for formic acid in our solid electrolyte cell design,

with consistently high FEs under a wide range of current densities (Fig. 5e,h). As shown in Table 1, CO$_2$RR to formate is a two-electron transfer process (the same as CO), but it only produces one OH$^-$ ion and the other charge is compensated by HCOO$^-$. As a result, the theoretical crossover CO$_2$ will be halved compared to the case of CO as seen from the theoretical guideline in Fig. 5k assuming a 100% formate FE. A slightly higher theoretical guideline was also included when taking into consideration our measured formate FEs with H$_2$ and CO as the byproducts. It is very interesting to observe that our measured CO$_2$ crossover rates, although very close, were consistently lower than the theoretical guideline with FE, which is different from the case of CO. This lower CO$_2$ crossover ratio could be due to the lower OH$^-$ ion density generated at the catalyst–membrane interface, which results in lower local pH and less carbonate formation. The total CO$_2$ recovery remained very close to both the measured and theoretical crossover CO$_2$, suggesting that the high

Fig. 7 | Improved CO₂ conversion via recycling crossover CO₂. a, Schematic of practical CO_2RR process using PSE reactor CO_2 recovery technology that ensures high carbon efficiency throughout the operation. This operation uses a three-port vessel to separate and collect headspace CO_2 gas while recycling saturated DI water back into the solid electrolyte layer. **b,** Carbon balance analysis on cathode side and middle layer of the solid electrolyte cell with changing inlet CO_2 flow rate. The electrolyser was operated at $100\,mA\,cm^{-2}$ with an electrode area of $5\,cm^2$. The inlet CO_2 flow rates were carefully calibrated (Methods). The cathode downstream CO_2 gas stream and the inlet was measured using the CO_2 meter while converted CO_2 was calculated using the FE. **c,** The FE and the continuous conversion of the Ag NW in a solid electrolyte with the CO_2 recycling system. FE was measured using the GC and continuous conversion efficiency was calculated by comparing CO_2 converted against the inlet CO_2 flow (Methods).

CO_2 recovery efficiency of our PSE reactor was not affected when anionic products were formed and transported across the AEM.

Last, CO_2 gas recovery during CO_2RR to multiple higher-value products was shown using commercial CuNPs as the catalyst that presents notable selectivity towards various multicarbon products[65,66]. The commercial CuNPs consisted of 30–50 nm diameter nanocrystals with uniform morphology (Fig. 5c and Supplementary Fig. 16). In our PSE reactor, this CuNP catalyst showed notable CO_2RR activity and selectivity for C_{2+} products especially at higher currents, delivering roughly 40% C_{2+} FE under $200\,mA\,cm^{-2}$ (Fig. 5f,i). For this CuNP sample, C_2H_4, CO and H_2 make up most of the products while $HCOO^-$ and CH_3COO^- together only have a FE of 10–14%, which results in Cu's CO_2 crossover rate not deviating too much from Ag NW or Ni-SAC, as shown by the theoretical guidelines (Fig. 5l). It is encouraging that our reactor still maintained a similarly high CO_2 recovery performance even under this more complicated scenario where the Cu catalyst produces up to seven different products including C_{2+} products, suggesting a wide applicability in CO_2RR fields in the future.

Water recycling system and long-term stability. In practical operations, a direct recovery of crossover CO_2 in its gas phase, instead of partially dissolved in water, is preferred and can be directly fed back to the main CO_2 stream. This can be achieved by continuously recycling the water stream through the PSE layer as shown in Supplementary Fig. 17. Continuous recycling of middle-layer

water can remove the need for dissolved CO_2 analysis since the liquid remains saturated with CO_2. Any further CO_2 gas crossover to the PSE layer after the first saturation will be extracted as pure gas. Using this setup, CO_2RR to CO on a Ag NW catalyst was continuously operated at 250 mA or $100\,mA\,cm^{-2}$ for practical CO_2 gas recovery demonstrations. As a visual demonstration, an empty balloon (roughly 100 ml in size) was filled with recovered CO_2 gas from the solid electrolyte layer after 90 minutes of operation, suggesting facile storage of recovered CO_2 gas (Fig. 6a,b and Supplementary Video 1). No visible change was seen in SEM images of Ag NW before and after this catalysis operation, indicating a good structure stability. To evaluate the long-term performance of gas recovery (Fig. 6c), the device was continuously operated for 750 hours without noticeable change in CO selectivity (roughly 90%) or cell voltage (roughly 3.5 V without iR compensation). During this stability test, the recovered CO_2 maintained relatively constant at around 1.4 to 1.5 sccm. Note here that this crossover rate is slightly lower than what we tested in Fig. 4 where we continuously flow in fresh DI water stream, which is because the CO_2 saturated DI water flow could backlash the CO_2/carbonate equilibrium and thus inhibit the carbonate formation at the catalyst–AEM interface. The gas crossover rate was also monitored during the long-term operation with noticeable measurement fluctuations, which may stem from the pressure fluctuations in the cathode and the solid electrolyte layer over the course of the stability test. For the entire duration, an average of roughly 80 to 90% crossover CO_2 measured from the cathode

side was recovered in the middle layer, showing consistent and efficient recovery potential of the device.

Recycling recovered CO_2 to improve CO_2 conversion efficiency. The recovered crossover CO_2 gas in our solid electrolyte reactor, if recycled back to the CO_2 input stream (Fig. 7a), could dramatically improve the continuous CO_2 conversion efficiency compared to that of the MEA reactor, which is typically limited to less than 50% (Table 1)[32]. To achieve a high continuous conversion efficiency that is defined as a proportion of supplied CO_2 continuously converted to products (Methods), we have to eliminate the excess of CO_2 gas supplied to the system. Therefore, while a 100 mA cm^{-2} cell current density (500 mA total current) was maintained, we gradually lowered the inlet CO_2 flow rate in our gas recycling system to monitor how it would affect the CO_2RR performance as well as the continuous conversion efficiency (Methods). Figure 7b presents the carbon balance analysis in this system, which includes how much CO_2 gas was converted to product and how much of it remained in the cathode-side outlet under different CO_2 gas supply flow rates. We observed that the CO FE was maintained at a relatively high level (roughly 85%) until the inlet CO_2 flow rate was decreased to 3.6 sccm, with the continuous conversion efficiency continuously increasing (Fig. 7c). This product selectivity decrease is mainly due to the lack of CO_2 reactant and thus water reduction to H_2 started to rise. By further reducing the CO_2 inlet flow rate, we obtained an impressive 91% continuous conversion efficiency while maintaining over 60% CO FE. The downstream remaining CO_2 flow rate was decreased to only 0.18 sccm, while the flow-out CO and H_2 was roughly 2.39 and 1.41 sccm, respectively, suggesting a low remaining CO_2 concentration of only 4.6%.

Conclusions

In this work, we demonstrated the use of PSE reactor design to successfully recover lost CO_2 gas during CO_2RR electrolysis while maintaining high catalytic performances. This work showed that traditional electrolysers have poor CO_2 use efficiency, which makes the process unsustainable. Adding a porous and ion-conducting solid electrolyte buffer layer, however, demonstrated that we were able to efficiently recover these carbon losses to ensure high CO_2 use efficiencies. This strategy avoids using extra gas separation equipment or energy required to separate crossover CO_2 from impurities, especially oxygen. Future studies can be done to further improve each component in the PSE reactor to make it more viable for practical CO_2 recovery during CO_2RR electrolysis, including optimizing the thickness of solid electrolyte layer for minimized ohmic drop and improving ion conductions between cathode and anode by designing different solid ion conductors.

Methods

Preparation of catalysts. Ag NW-L70 (ACS Material Store) used in this work was purchased from the vendor and was stored suspended in water. CuNP (Sigma-Aldrich), described as commercial copper in this work, was purchased directly from the vendor. 2D-Bi nanosheet NP was synthesized following our previous study that showed this material's high selectivity towards formic acid[53]. Ni-SAC was also prepared following the previous work to disperse Ni atoms onto a graphene nanosheets well[59]. Ag NP (Sky-Spring Nanomaterials) was also directly purchased directly from the vendor. For the preparation of the cathode electrode, 40 mg of the target catalyst with 160 μl of Nafion 117 polymer binder solution (Sigma-Aldrich, 5%) was suspended in 4 ml of isopropyl alcohol to prepare roughly 10 mg ml^{-1} catalyst ink. This ink was sonicated for about 30 min and then was spray coated on to the Sigracet 28BC GDL electrode (Fuel Cell Store) to obtain roughly 0.8 mg cm^{-2} catalyst deposition on the GDL. An IrO$_2$ electrode (Dioxide Materials) and nickel foam were used for the anode electrode during the electrochemical process.

Electrochemical CO_2 reduction. Electrochemical measurements were all conducted using a Bio-Logic VMP3 workstation. The MEA cell consists of Ag NW catalyst loaded on 2.5 cm^2 GDL as the cathode. A 0.5-mm thick polytetrafluoroethylene (PTFE) gasket with a 2.5 cm^2 window and the AEM membrane separates the cathode from the Ni foam (Supplementary Fig. 2) or

IrO_2 (Supplementary Fig. 12) anode. The components of the electrochemical cell were compressed together mechanically using eight pairs of nuts and bolts with hand tightening. In the MEA CO_2 recovery test, the cathode was supplied with 20 sccm of humified CO_2 gas using a 50-sccm-range MFC (Alicat Scientific MFC) and the anode was supplied with recycled 0.5 M KHCO$_3$ solution (Supplementary Fig. 2) via a peristaltic pump (Huiyu peristaltic pump). The recycled anolyte was constantly bubbled with 50 sccm Ar carrier gas flow and the headspace gases were vented into the GC (SRI 8010C) for anode side gas analysis. For the MEA IV test for a direct comparison with the solid electrolyte reactor (Supplementary Fig. 12), an IrO_2 anode was recycled with DI water or 0.1 M K$_2$SO$_4$.

The PSE reactor used the catalysts Ag NW, Ag NP, Ni-SAC, 2D-Bi or CuNPs loaded on 2.5 cm^2 GDL as the cathode electrode. A 0.5-mm thick PTFE gasket with a 2.5 cm^2 window and AEM membrane was placed between the cathode electrode and the solid electrolyte layer. The middle layer solid electrolyte compartment was made of 2.5 mm Delrin plastic (1.5 mm for the thin plate solid electrolyte reactor in Supplementary Information and Supplementary Fig. 13). This plastic layer had a 2.5×2.5 cm window in which we 'packed' approximately 1 g of the proton conducting polymer electrolyte, Dowex 50W X8 hydrogen form (Sigma-Aldrich), as shown in Supplementary Fig. 4. Nafion 117 film (Fuel Cell Store) with a second PTFE gasket with 6.25 cm^2 window was used to separate the anode from the middle solid electrolyte layer. IrO_2 was used as the anode for the OER. All the above-mentioned components of the electrochemical cell were compressed together mechanically using eight pairs of nuts and bolts with hand tightening. During the operation of the solid electrolyte reactor without DI water recycling system (Figs. 3b–5), the cathode was supplied with 20 sccm humidified CO_2 for all tests. When the FE for the Cu sample was tested, the flow rate of inlet CO_2 was temporarily increased to 50 sccm to minimize the FE measurement error associated with CO_2 stream flow rate change. The middle solid electrolyte layer was continuously flowed with 1.1 ml min^{-1} of a DI water stream to bring out dissolved CO_2 and CO_2 gas, and the anode side was circulated with 2.7 ml min^{-1} of 0.5 M H$_2$SO$_4$. Before any of the selectivity or performance reading was tested, the cell was activated by running a low current through the device for roughly 20 min before measuring its cell voltage and its selectivity. In the case of solid electrolyte layer with a recycled DI water stream (Fig. 6), the anolyte was replaced with 2.7 ml min^{-1} of DI water while everything else was conducted with the same parameters.

For CO_2 recycling and continuous conversion efficiency testing, some of the parameters were varied. A 5 cm^2 cathode electrode was used and 100 mA cm^{-2} was used in the recycling system. The CO_2 gas inlet was not directly connected to the cathode, instead it was bubbled into the middle-layer liquid chamber first, where it combined with the recovered CO_2 before being inserted into the cathode inlet. Depending on the targeted flow rate, CO_2 gas flow rate was adjusted by MFC, however, the actual flow rate of the gas was further calibrated by a CO_2 meter (CO2Meter.com).

All cell resistance was measured by potentiostatic electrochemical impedance spectroscopy and all the whole cell voltages were reported without any iR compensation. The typical impedance of our solid electrolyte reactor was measured to be roughly 1 to 3 Ω including electrical connections to the instrument.

Output gas and liquid analysis. All the gas supply flow rates (CO_2, Ar, C_2H_4 and CH_4) were precisely controlled by MFCs (Alicat Scientific) with different ranges. For example, our 20-sccm inlet CO_2 was controlled by a 50-sccm range MFC. On the basis of the MFC product information, it had an accuracy of ±0.8% of reading + 0.2% of full scale, which gave us a small error range of ±0.26 sccm when supplying a 20 sccm CO_2 stream (roughly 1% error). Cathode-side downstream gas was mixed with 200 sccm of Ar carrier gas and 5 sccm of internal standard gas, which was CH_4 for copper testing and C_2H_4 for all other tests. This mixture was then fed to the GC (SRI 8010C) where a flame ionization detector with methanizer was used for CO_2 quantity analysis and a thermal conductivity detector was used for O_2 quantity analysis. The output signal contained CO_2 and a internal standard gas peak that were integrated for their areas. The ratio between these two areas gave the actual downstream CO_2 flow rate using the following equations:

$$R_{C_2H_4 \text{ or } CH_4} = \frac{(CO_2 \text{ peak area})}{(C_2H_4 \text{ or } CH_4 \text{ peak area})}, \qquad (1)$$

$$M = 12.858705\,(C_2H_4)\,,\, 6.3941\,(CH_4)\,,\quad b = 1.701189\,(C_2H_4)\,,\, -0.151\,(CH_4) \qquad (2)$$

where $R_{C_2H_4 \text{ or } CH_4}$ is the ratio between CO_2 peak area and the internal gas used, M is the slope of the calibration line and b is the intercept of the calibration line. As shown above, depending on the internal gas used, the calibration values are different (Supplementary Fig. 6). This downstream CO_2 flow rate measurement method was compared with the measurement done by directly placing a MFC on the outlet. For most of the cell current range, GC measurement is more sensitive to CO_2 'lost' and more reliable than MFC measurement during the process comparatively (Supplementary Fig. 5).

For CO_2RR gas product analysis, we directly flowed the downstream gas, without mixing with carrier gas or internal standard gas, into the GC

(Shimadzu GC 2014). The partial current of the measured gas product is calculated by following equation:

$$j_i = x_i \times v \times \frac{n_i F p^0}{RT} \times A^{-1} \tag{3}$$

where x_i is the volume fraction of the product determined by online GC referenced to calibration curves from the standard gas sample, v is the flow rate of 20 sccm, n_i is the number of electrons involved, $p^0 = 101.3$ kPa, F is the Faradaic constant, $T = 298$ K and R is the gas constant. FE is then calculated using equation (4):

$$FE = \frac{j_i}{j_{overall}} \times 100\% \tag{4}$$

Since the downstream gas flow rate on the cathode side is changed due to the CO_2 gas conversion or crossover, selectivity of H_2 and CO in Ag NW, Ag NP and Ni-SAC we obtained from the GC (calculated under the assumption that total flow rate of downstream gas is still 20 sccm) was later normalized to 100% after carefully confirming the absence of other gas or liquid products. In the case of the CuNPs where multiple CO_2RR products were cogenerated, the selectivity was tested with increased input CO_2 flow rate to minimize the error arising from flow rate discrepancy in the GC instead of normalization.

One-dimensional 1H nuclear magnetic resonance (NMR) spectra measured using a Bruker AVIII 500 MHz NMR spectrometer was used to quantify the liquid product from the commercial CuNPs and 2D-Bi catalyst test. For the NMR test, 500 μl of the middle-layer output liquid was mixed with 100 μl of D_2O (Sigma-Aldrich, 99.9 at%D) and 0.05 μl of dimethyl sulfoxide (Sigma-Aldrich, 99.9 at%D) as the internal standard.

CO_2 saturated 0.05 M H_2SO_4 was used as the solvent during the water displacement measurement to measure the CO_2 bubble flow rate in the heterogenous middle-layer downstream flow. Acid was used because CO_2 gas has lower solubility in acidic solutions, and it was also presaturated with CO_2 to minimize gas dissolution during the bubble flow rate measuring process. This water displacement showed high measurement accuracy (Supplementary Fig. 9). The dissolved CO_2 in the liquid was measured using a titration method (Supplementary Fig. 7).

The middle-layer output stream containing dissolved CO_2 was collected directly in 200–500 μl of 1 M NaOH (volume of NaOH is changed to ensure the pH of the collected solution would be greater than ten). By collecting them into the alkaline solution, the loss of dissolved CO_2 to air was minimized and a full range of titrations could be conducted. Then 5 ml of this liquid was titrated using 0.1 M HCl and a pH meter (Orion Star A111). By recording and graphing the titration data, we can find amount of HCl liquid required to go from one equivalence point to the other. This determines how many moles of carbonate species exist inside the liquid samples and we can plug this value into equation (5) to retrieve the CO_2 flow rate equivalent of dissolved carbon concentration.

$$Q = \frac{\Delta V \times c \times 24.4 \frac{L}{mol}}{v} \times q \tag{5}$$

where Q is the CO_2 flow rate equivalent of dissolved carbon concentration, ΔV is the volume of HCl liquid used to change the titrant's pH from its first equivalence point to the next during titration, c is the concentration of the HCl solution used, v is the volume of the sample titrated and q is the flow rate of the collected liquid output.

For the CO_2 recycle and continuous conversion efficiency investigation, the CO_2 gas flow rate was measured using a CO_2 meter. The outlet of the cathode stream was diluted with 100 sccm of argon and was fed into the CO_2 meter for accurate concentration reading. The inlet flow and outlet during operation was measured to get the difference in the CO_2 flow rate. Also, CO_2 converted measurement was calculated using FE for CO.

Continuous conversion efficiency is defined as amount inlet CO_2 that is continuously converted to the desired product. The FE information from the GC was used to calculate this value following the equation below:

$$\text{Continuous conversion efficiency} = \frac{i_{CO}}{n_{CO} \times F \times \text{inlet gas flow rate (sccm)}} \times \frac{60 \text{ s}}{1 \text{ min}}$$
$$\times 24{,}400 \frac{cm^3}{mol} \tag{6}$$

where $i_{CO}i$ is partial current of CO and n_{CO} is the electron transfer number for CO_2 reduction to CO.

Data availability

References

1. Bushuyev, O. S. et al. What should we make with CO_2 and how can we make it? *Joule* **2**, 825–832 (2018).
2. Aresta, M., Dibenedetto, A. & Angelini, A. Catalysis for the valorization of exhaust carbon: from CO_2 to chemicals, materials, and fuels. technological use of CO_2. *Chem. Rev.* **114**, 1709–1742 (2014).
3. Centi, G., Quadrelli, E. A. & Perathoner, S. Catalysis for CO_2 conversion: a key technology for rapid introduction of renewable energy in the value chain of chemical industries. *Energ. Environ. Sci.* **6**, 1711–1731 (2013).
4. Olah, G. A., Prakash, G. K. S. & Goeppert, A. Anthropogenic chemical carbon cycle for a sustainable future. *J. Am. Chem. Soc.* **133**, 12881–12898 (2011).
5. Liu, X. Y. et al. Understanding trends in electrochemical carbon dioxide reduction rates. *Nat. Commun.* **8**, 15438 (2017).
6. Nitopi, S. et al. Progress and perspectives of electrochemical CO_2 reduction on copper in aqueous electrolyte. *Chem. Rev.* **119**, 7610–7672 (2019).
7. Rosen, J. et al. Mechanistic insights into the electrochemical reduction of CO_2 to CO on nanostructured Ag surfaces. *ACS Catal.* **5**, 4293–4299 (2015).
8. Kortlever, R., Shen, J., Schouten, K. J., Calle-Vallejo, F. & Koper, M. T. Catalysts and reaction pathways for the electrochemical reduction of carbon dioxide. *J. Phys. Chem. Lett.* **6**, 4073–4082 (2015).
9. Higgins, D., Hahn, C., Xiang, C. X., Jaramillo, T. F. & Weber, A. Z. Gas-diffusion electrodes for carbon dioxide reduction: a new paradigm. *ACS Energy Lett.* **4**, 317–324 (2019).
10. Ren, S. X. et al. Molecular electrocatalysts can mediate fast, selective CO_2 reduction in a flow cell. *Science* **365**, 367–369 (2019).
11. Yan, Z. F., Hitt, J. L., Zeng, Z. C., Hickner, M. A. & Mallouk, T. E. Improving the efficiency of CO_2 electrolysis by using a bipolar membrane with a weak-acid cation exchange layer. *Nat. Chem.* **13**, 33–40 (2021).
12. Gu, J., Hsu, C. S., Bai, L., Chen, H. M. & Hu, X. Atomically dispersed Fe(3+) sites catalyze efficient CO_2 electroreduction to CO. *Science* **364**, 1091–1094 (2019).
13. Wu, Y., Jiang, Z., Lu, X., Liang, Y. & Wang, H. Domino electroreduction of CO_2 to methanol on a molecular catalyst. *Nature* **575**, 639–642 (2019).
14. Delacourt, C., Ridgway, P. L., Kerr, J. B. & Newman, J. Design of an electrochemical cell making syngas (CO+H-2) from CO_2 and H_2O reduction at room temperature. *J. Electrochem. Soc.* **155**, B42–B49 (2008).
15. Phillips, K. R., Katayama, Y., Hwang, J. & Shao-Horn, Y. Sulfide-derived copper for electrochemical conversion of CO_2 to formic acid. *J. Phys. Chem. Lett.* **9**, 4407–4412 (2018).
16. Sen, S., Brown, S. M., Leonard, M. & Brushett, F. R. Electroreduction of carbon dioxide to formate at high current densities using tin and tin oxide gas diffusion electrodes. *J. Appl. Electrochem.* **49**, 917–928 (2019).
17. Ma, W. et al. Promoting electrocatalytic CO_2 reduction to formate via sulfur-boosting water activation on indium surfaces. *Nat. Commun.* **10**, 892 (2019).
18. Lin, S. et al. Covalent organic frameworks comprising cobalt porphyrins for catalytic CO_2 reduction in water. *Science* **349**, 1208–1213 (2015).
19. Ma, W. C. et al. Electrocatalytic reduction of CO_2 to ethylene and ethanol through hydrogen-assisted C-C coupling over fluorine-modified copper. *Nat. Catal.* **3**, 478–487 (2020).
20. Dinh, C. T. et al. CO_2 electroreduction to ethylene via hydroxide-mediated copper catalysis at an abrupt interface. *Science* **360**, 783–787 (2018).
21. Choi, C. et al. Highly active and stable stepped Cu surface for enhanced electrochemical CO_2 reduction to C_2H_4. *Nat. Catal.* **3**, 804–812 (2020).
22. Li, J. et al. Copper adparticle enabled selective electrosynthesis of n-propanol. *Nat. Commun.* **9**, 4614 (2018).
23. Pang, Y. J. et al. Efficient electrocatalytic conversion of carbon monoxide to propanol using fragmented copper. *Nat. Catal.* **2**, 251–258 (2019).
24. Dinh, C. T., de Arquer, F. P. G., Sinton, D. & Sargent, E. H. High rate, selective, and stable electroreduction of CO_2 to CO in basic and neutral media. *ACS Energy Lett.* **3**, 2835–2840 (2018).
25. Weng, L. C., Bell, A. T. & Weber, A. Z. Towards membrane-electrode assembly systems for CO_2 reduction: a modeling study. *Energy Environ. Sci.* **12**, 1950–1968 (2019).
26. Kucernak, A., Bidault, F. & Smith, G. Membrane electrode assemblies based on porous silver electrodes for alkaline anion exchange membrane fuel cells. *Electrochim. Acta* **82**, 284–290 (2012).
27. Hori, Y., Ito, H., Okano, K., Nagasu, K. & Sato, S. Silver-coated ion exchange membrane electrode applied to electrochemical reduction of carbon dioxide. *Electrochim. Acta* **48**, 2651–2657 (2003).
28. Kim, C. et al. Achieving selective and efficient electrocatalytic activity for CO_2 reduction using immobilized silver nanoparticles. *J. Am. Chem. Soc.* **137**, 13844–13850 (2015).
29. Wu, J. et al. Achieving highly efficient, selective, and stable CO_2 reduction on nitrogen-doped carbon nanotubes. *ACS Nano* **9**, 5364–5371 (2015).
30. Pan, Y. et al. Design of single-atom Co-N5 Catalytic Site: a robust electrocatalyst for CO_2 reduction with nearly 100% CO selectivity and remarkable stability. *J. Am. Chem. Soc.* **140**, 4218–4221 (2018).

31. Cheng, W. H. et al. CO$_2$ reduction to CO with 19% efficiency in a solar-driven gas diffusion electrode flow cell under outdoor solar illumination. *ACS Energy Lett.* **5**, 470–476 (2020).

32. Jeng, E. & Jiao, F. Investigation of CO$_2$ single-pass conversion in a flow electrolyzer. *React. Chem. Eng.* **5**, 1768–1775 (2020).

33. Larrazabal, G. O. et al. Analysis of mass flows and membrane cross-over in CO$_2$ reduction at high current densities in an MEA-type electrolyzer. *ACS Appl. Mater. Interfaces* **11**, 41281–41288 (2019).

34. Lin, M., Han, L. H., Singh, M. R. & Xiang, C. X. An experimental- and simulation-based evaluation of the CO$_2$ utilization efficiency of aqueous-based electrochemical CO$_2$ reduction reactors with ion-selective membranes. *Acs Appl Energ. Mater.* **2**, 5843–5850 (2019).

35. Liu, Z. C., Yang, H. Z., Kutz, R. & Masel, R. I. CO$_2$ electrolysis to CO and O-2 at high selectivity, stability and efficiency using sustainion membranes. *J. Electrochem. Soc.* **165**, J3371–J3377 (2018).

36. Ma, M., Kim, S., Chorkendorff, I. & Seger, B. Role of ion-selective membranes in the carbon balance for CO$_2$ electroreduction via gas diffusion electrode reactor designs. *Chem. Sci.* **11**, 8854–8861 (2020).

37. Parrondo, J. et al. Degradation of anion exchange membranes used for hydrogen production by ultrapure water electrolysis. *RSC Adv.* **4**, 9875–9879 (2014).

38. Patru, A., Binninger, T., Pribyl, B. & Schmidt, T. J. Design principles of bipolar electrochemical Co-electrolysis cells for efficient reduction of carbon dioxide from gas phase at low temperature. *J. Electrochem. Soc.* **166**, F34–F43 (2019).

39. Rabinowitz, J. A. & Kanan, M. W. The future of low-temperature carbon dioxide electrolysis depends on solving one basic problem. *Nat. Commun.* **11**, 5231 (2020).

40. Reinisch, D. et al. Various CO$_2$-to-CO electrolyzer cell and operation mode designs to avoid CO$_2$-crossover from cathode to anode. *Z. Phys. Chem.* **234**, 1115–1131 (2020).

41. Ripatti, D. S., Veltman, T. R. & Kanan, M. W. Carbon monoxide gas diffusion electrolysis that produces concentrated C-2 products with high single-pass conversion. *Joule* **3**, 240–256 (2019).

42. Zhou, X. H. et al. Solar-driven reduction of 1 atm CO$_2$ to formate at 10% energy-conversion efficiency by use of a TiO$_2$-Protected III-V tandem photoanode in conjunction with a bipolar membrane and a Pd/C cathode electrocatalyst. *ECS Trans.* **77**, 31–41 (2017).

43. Huang, J. E. et al. CO$_2$ electrolysis to multicarbon products in strong acid. *Science* **372**, 1074–1078 (2021).

44. O'Brien, C. et al. Single pass CO$_2$ conversion exceeding 85% in the electrosynthesis of multicarbon products via local CO$_2$ regeneration. *ACS Energy Lett.* **6**, 2952 (2021).

45. Hatsukade, T., Kuhl, K. P., Cave, E. R., Abram, D. N. & Jaramillo, T. F. Insights into the electrocatalytic reduction of CO$_2$ on metallic silver surfaces. *Phys. Chem. Chem. Phys.* **16**, 13814–13819 (2014).

46. Luan, C. H. et al. High-performance carbon dioxide electrocatalytic reduction by easily fabricated large-scale silver nanowire arrays. *ACS Appl. Mater. Inter.* **10**, 17950–17956 (2018).

47. Zhao, S., Jin, R. X. & Jin, R. C. Opportunities and challenges in CO$_2$ reduction by gold- and silver-based electrocatalysts: From bulk metals to nanoparticles and atomically precise nanoclusters. *ACS Energy Lett.* **3**, 452–462 (2018).

48. Bandara, T. M. et al. Effect of the alkaline cation size on the conductivity in gel polymer electrolytes and their influence on photo electrochemical solar cells. *Phys. Chem. Chem. Phys.* **18**, 10873–10881 (2016).

49. Endrodi, B. et al. Operando cathode activation with alkali metal cations for high current density operation of water-fed zero-gap carbon dioxide electrolyzers. *Nat. Energy* **6**, 439–448 (2021).

50. Wang, R. M. et al. Maximizing Ag utilization in high-rate CO$_2$ electrochemical reduction with a coordination polymer-mediated gas diffusion electrode. *ACS Energy Lett.* **4**, 2024–2031 (2019).

51. Fan, L., Xia, C., Zhu, P., Lu, Y. Y. & Wang, H. T. Electrochemical CO$_2$ reduction to high-concentration pure formic acid solutions in an all-solid-state reactor. *Nat. Commun.* **11**, 3633 (2020).

52. Xia, C., Xia, Y., Zhu, P., Fan, L. & Wang, H. Direct electrosynthesis of pure aqueous H$_2$O$_2$ solutions up to 20% by weight using a solid electrolyte. *Science* **366**, 226–231 (2019).

53. Xia, C. et al. Continuous production of pure liquid fuel solutions via electrocatalytic CO$_2$ reduction using solid-electrolyte devices. *Nat. Energy* **4**, 776–785 (2019).

54. Yang, H., Kaczur, J. J., Sajjad, S. D. & Masel, R. I. CO$_2$ conversion to formic acid in a three compartment cell with sustainion (TM) membranes. *ECS Trans.* **77**, 1425–1431 (2017).

55. Zhu, P. et al. Direct and continuous generation of pure acetic acid solutions via electrocatalytic carbon monoxide reduction. *P Natl Acad. Sci. USA* **118**, e2010868118 (2021).

56. Matin, N. S., Remias, J. E., Neathery, J. K. & Liu, K. L. Facile method for determination of amine speciation in CO$_2$ capture solutions. *Ind. Eng. Chem. Res.* **51**, 6613–6618 (2012).

57. Pinho, C. The positive displacement method for calibration of gas flow meters. The influence of gas compressibility. *Appl. Therm. Eng.* **41**, 111–115 (2012).

58. Wiebe, R. & Gaddy, V. L. The solubility of carbon dioxide in water at various temperatures from 12 to 40 degrees and at pressures to 500 atmospheres—critical phenomena. *J. Am. Chem. Soc.* **62**, 815–817 (1940).

59. Jiang, K. et al. Isolated Ni single atoms in graphene nanosheets for high-performance CO$_2$ reduction. *Energ. Environ. Sci.* **11**, 893–903 (2018).

60. Zhao, C. et al. Ionic exchange of metal-organic frameworks to access single nickel sites for efficient electroreduction of CO$_2$. *J. Am. Chem. Soc.* **139**, 8078–8081 (2017).

61. Yang, H. B. et al. Atomically dispersed Ni(i) as the active site for electrochemical CO$_2$ reduction. *Nat. Energy* **3**, 140–147 (2018).

62. Zheng, T. T. et al. Large-scale and highly selective CO$_2$ electrocatalytic reduction on nickel single-atom catalyst. *Joule* **3**, 265–278 (2019).

63. Jiang, K. et al. Transition-metal single atoms in a graphene shell as active centers for highly efficient artificial photosynthesis. *Chem.* **3**, 950–960 (2017).

64. Gong, Q. F. et al. Structural defects on converted bismuth oxide nanotubes enable highly active electrocatalysis of carbon dioxide reduction. *Nat. Commun.* **10**, 2807 (2019).

65. Kim, D., Kley, C. S., Li, Y. F. & Yang, P. D. Copper nanoparticle ensembles for selective electroreduction of CO$_2$ to C-2-C-3 products. *Proc. Natl Acad. Sci. USA* **114**, 10560–10565 (2017).

66. Loiudice, A. et al. Tailoring copper nanocrystals towards C-2 products in electrochemical CO$_2$ reduction. *Angew. Chem. Int Ed.* **55**, 5789–5792 (2016).

Acknowledgements

Author contributions

H.W. supervised the project. J.Y.T.K., P.Z. and H.W. designed the research. J.Y.T.K. and P.Z. performed the research. F.-Y.C., Z.-Y.W. and D.A.C. contributed new reagents/analytic tools. J.Y.T.K., P.Z., F.-Y.C., Z.-Y.W., D.A.C. and H.W. analysed the data. J.Y.T.K., P.Z. and H.W. wrote the paper.

Competing interests

The authors declare no competing interests.

Additional information

Supplementary information The online version contains supplementary material available at https://doi.org/10.1038/s41929-022-00763-w.

Correspondence and requests for materials should be addressed to Haotian Wang.

Peer review information *Nature Catalysis* thanks Sarah Lamaison, Hongyan Liang and the other, anonymous, reviewer(s) for their contribution to the peer review of this work.

Reprints and permissions information is available at www.nature.com/reprints.

Publisher's note Springer Nature remains neutral with regard to jurisdictional claims in published maps and institutional affiliations.